# Supplement to: **Formulating multi-cellular models of metabolism in tissues: application to energy metabolism in the human brain**

Nathan E. Lewis[1], Gunnar Schramm[4,5], Aarash Bordbar[1], Jan Schellenberger [2], Michael Paul Andersen[1], Jeff K. Cheng[1], Nilam K. Patel[1], Alex Yee[1], Randall A. Lewis[3], Roland Eils[4,5], Rainer König[4,5], Bernhard Ø. Palsson[1]

[1]Department of Bioengineering and [2]Bioinformatics Program, University of California San Diego, 417 Powell-Focht Bioengineering Hall, 9500 Gilman Drive, La Jolla, CA, 92093-0412, USA

[3]Department of Economics, Massachusetts Institute of Technology, 50 Memorial Drive, E52-391, Cambridge, MA, 02142, USA

[4]Department of Bioinformatics and Functional Genomics, Institute of Pharmacy and Molecular Biotechnology, and Bioquant, University of Heidelberg, Im Neuenheimer Feld 267, 69120 Heidelberg, Germany

[5]Department of Theoretical Bioinformatics, German Cancer Research Center (DKFZ), Im Neuenheimer Feld 280, 69120 Heidelberg, Germany

# Supplementary Methods and Analysis

## *Monte Carlo sampling*

Monte Carlo Sampling was used to generate a set of uniform, feasible flux distributions (points). The method is based on the Artificially Centered Hit and Run (ACHR) algorithm with slight modifications [1]. Initially a set of non-uniform pseudo-random points, called warm-up points, is generated. In a series of iterations, each point is randomly moved, always remaining within the feasible flux space. This is done by 1) choosing a random direction, 2) computing the limits of how far one can travel in that direction and 3) choosing a new point randomly along this line. After numerous iterations, the set of points is mixed and approaches a uniform sample of the solution space.

Warm-up points are generated by Linear Programming (LP). For each point, the objective coefficients are set to a random vector with values in [-1,1]. This generates a point at random corners in the solution space.

The direction of movement is chosen as described in [2]. The center point of all points is computed and the direction is the difference of a randomly selected point and the center point. This has the effect of biasing the directions in the longer directions of the solution space and speeds up the rate of mixing while maintaining sample uniformity.

One of the problems with the ACHR is that the termination condition is not clearly defined. Here we introduce the concept of the mixed fraction as a measure of the number of iterations required for proper mixing. A partition is created over the set of points by drawing a line at the median value with half the points on either side of the line. The mixed fraction is a count of how many points cross this line between the beginning of sampling and the end as a fraction of the total number of points. Initially the mixed fraction is 1 as all points are on the same side of the partition. When perfect mixing is achieved, each point has a 50% chance of crossing the partition line so the mixed fraction will be close to 0.5. This value is approached asymptotically and a threshold of 0.51 was used for sampling.

## *Additional effects to metabolic capacity and neurotransmission with various AD-associated enzyme deficiencies*

A few central metabolic enzymes demonstrate altered expression or activity in AD, such as pyruvate dehydrogenase (PDHm), α-ketoglutarate dehydrogenase (AKGDm), and cytochrome c oxidase (CYOO) [3, 4]. While α-ketoglutarate dehydrogenase was discussed more heavily in this work, due to its 57% decrease in activity in post mortem brain, pyruvate dehydrogenase and cytochrome c oxidase also show decreased activity that leads to suppressed metabolic network activity.

To test the additional two enzymes, the models were provided cerebral metabolic rates as reported for healthy elderly patients [5, 6], in an effort to measure the change from normal brain metabolism to the more constrained metabolism in Alzheimer's disease. In our models, pyruvate dehydrogenase flux was reduced by 41% from its normal flux, as reported in [4], and cytochrome c oxidase was reduced by 30% from its normal flux (no enzymatic assays have reported the actual level of decreased flux in Alzheimer's disease in human). *In silico*, the decreased activity of these enzymes shows metabolic capacity impairments in neurons. That is, the rate of $CO_2$ efflux decreases significantly when cytochrome c oxidase or pyruvate dehydrogenase is inhibited (Supplementary Figures 1.a-b). Moreover, deficiencies in PDHm activity leads to a decrease in allowable cholinergic neurotransmission capacity ($p = 0.032$; Supplementary Figure 1.c).

Similar tests were done on the Çakır [7] model and the entire human reconstruction (HR1). The Çakır model is unable to withstand the 41% PDHm knock-down. However, a 10% decrease in PDHm surprisingly reduces cholinergic neuron neurotransmission capacity by 89%, while it reduces the median rate of $CO_2$ efflux by less than 1%. When PDHm is knocked down in the HR1 model, the median rate of $CO_2$ efflux also does not decrease. However, the comparison of cholinergic neurotransmission rate in the HR1 model is not feasible because choline acetyltransferase participates in a type 3 extreme pathway, or "loop" [8], in the model. When cytochrome c oxidase is suppressed, it only shows a 1% decrease in the rate of $CO_2$ efflux in the Çakır model, and no significant decrease in the HR1 model.

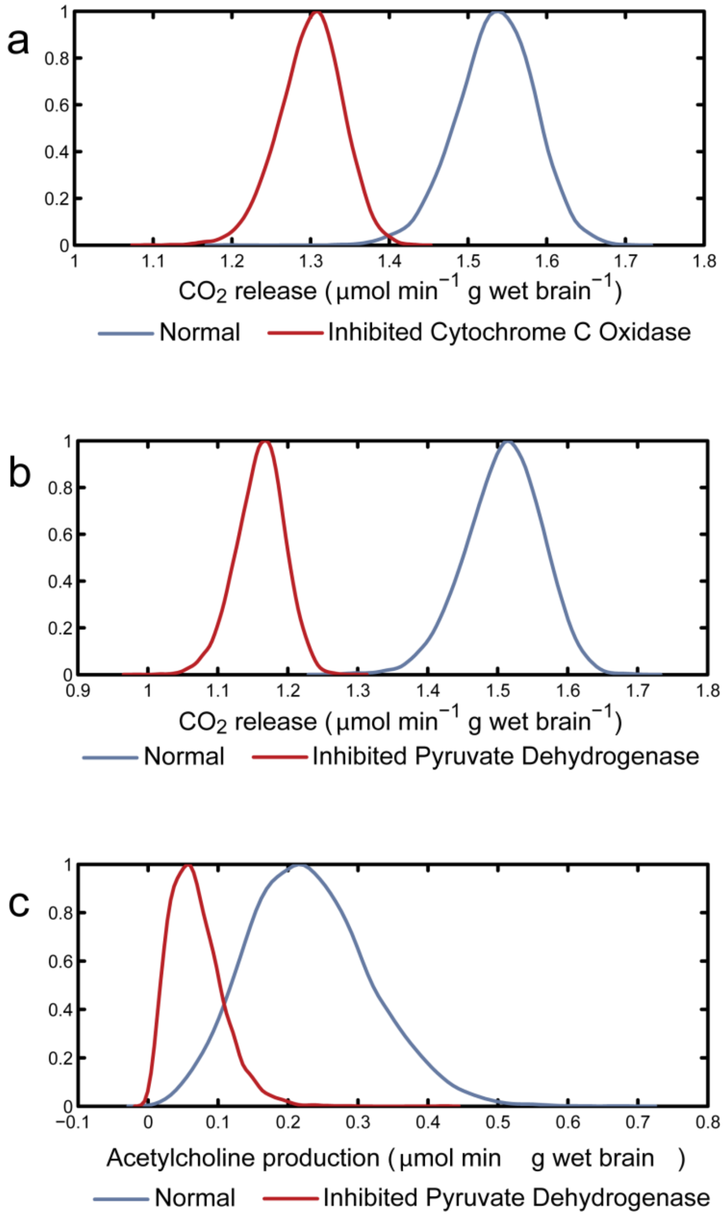

**Supplementary Figure 1. Pyruvate dehydrogenase and cytochrome c oxidase deficiencies in AD effect neuronal functions.** As seen in α-ketoglutarate dehydrogenase deficiencies, there are decreased feasible metabolic rates for brain with inhibition of (a) cytochrome c oxidase and (b) pyruvate dehydrogenase. In addition, (c) inhibition of pyruvate dehydrogenase significantly decreases the allowable acetylcholine production rate. Cytochrome c oxidase inhibition shown here was done in the glutamatergic neuron model, and pyruvate dehydrogenase inhibition was done in the cholinergic neuron model. However, results were the same irrespective of the model choice.

## *A comparison of GAD and other neuron specific genes in control and AD patients*

As demonstrated in Figure 3 in the main text, the use of our model aided in the prediction that GAD can play a neuroprotective role in specific neuron populations in Alzheimer's disease. In addition, our model provided the mechanism by which it plays this role. Further analysis is shown here to further support our model-derived hypothesis.

A comparison of the regional expression levels correlates better with Alzheimer's disease pathology than other neuron-specific genes. To test this, all other known neuron-specific genes were subjected to the same analysis as for GAD. Specifically, the distribution of each neuron-specific gene across six brain regions was assessed to see if the expression follows the same pattern as seen in Alzheimer's disease. Each neuron-specific gene was normalized against the three remaining neuron-specific genes (similar to GAD normalization described in the methods section). As seen in Supplementary Figure 2.b-e, no other neuron-specific genes tested here demonstrated an expression pattern consistent with the pattern of damage susceptibility. However, in control brain, GAD shows higher expression per neuron in brain regions that are relatively unaffected in AD, and lower expression in affected regions (Supplementary Figure 2.a). In addition, it is expected that any genes providing a neuroprotective role, or that increase neuron susceptibility, would either show an increase or decrease, respectively, in expression per neuron in AD patients. However, none of these neuron specific genes show such this trend (Supplementary Figure 2.b-e), except for GAD (Supplementary Figure 2.a).

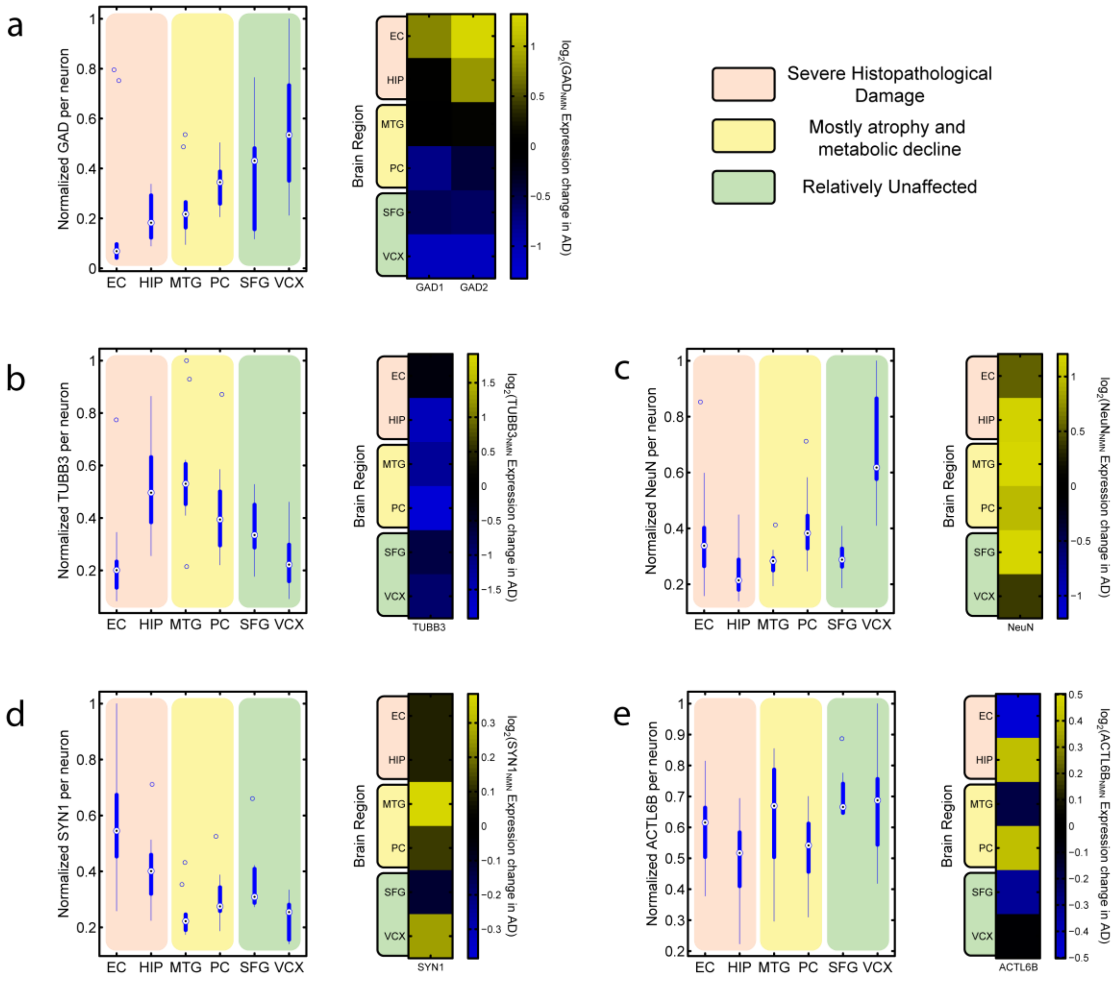

**Supplementary Figure 2. Other neuron-specific genes do not show regional specificity in expression consistent with AD pathology.** GAD expression shows a regional specificity consistent with Alzheimer's disease pathology. (a) Specifically, regions with severe damage show the lowest expression levels in control brain, while relatively unaffected regions show higher expression. Moreover, in AD, regions that are the most severely affected show an increase in the amount of GAD per neuron, while unaffected regions do not, suggesting that GAD may play a neuroprotective role as predicted by the model. The four other neuron-specific genes, i.e., (b) TUBB3, (c) NeuN, (d) SYN1, and (e) ACTL6B, were all assessed in a similar manner and none of them demonstrated a similar pattern, thereby providing additional support for the role of GAD.

## *DLX genes also correlate with AD pathology*

The DLX genes are a class of genes that are highly expressed in the developing brain, and the DLX1, DLX2, DLX5 and DLX6 isoforms are known to be expressed in primarily in GABAergic neurons. Interestingly, these genes also show a similar (although weaker) expression pattern as seen with GAD (Supplementary Figure 3). This, however, is not surprising since it has been shown the DLX2 and DLX5 isoforms induce GAD expression in the brain while DLX1 aids in the differentiation into GABAergic neurons [9, 10]. Consistent with this, DLX2 and DLX5 show the greatest increase of expression in the brain regions that show the most damage in AD, thereby providing additional support that GAD may be playing a neuroprotective role.

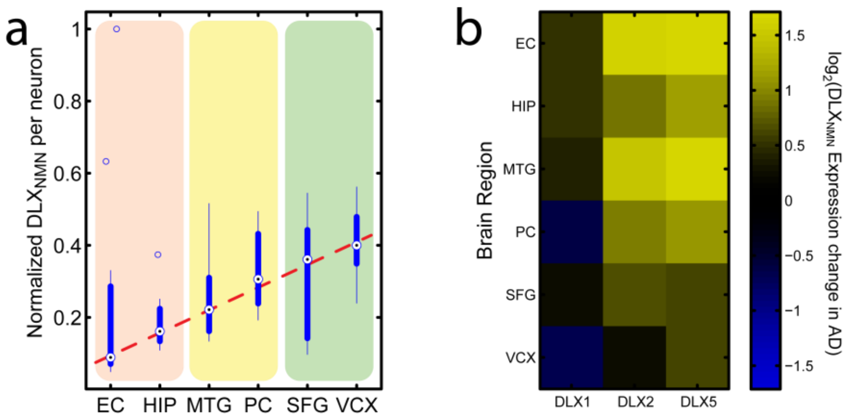

**Supplementary Figure 3. The DLX genes show an expression pattern similar to that of GAD.** The DLX genes were tested to provide additional support to the model predictions of GAD being neuroprotective. These genes, which are found to be expressed in GABAergic neurons, show a similar regional expression pattern as GAD, although weaker, in control brain (a) and an increased expression level per neuron in AD (b). The stronger results for DLX2 and DLX5 are especially supportive of GAD's contribution as these are known to induce GAD expression.

## *GAD expression patterns are robust against neuron marker choice*

None of the neuron marker genes chosen for the analysis in this study have been known to be differentially expressed non-histopathologically affected neurons in Alzheimer's disease. The only exception is TUBB3, which has only been suggested to be down-regulated in one study which used the same set of microarrays as used here [11]. However, the usage of four neuron markers representing different parts of the cell attempts to buffer against unknown changes of individual neuron markers, under the assumption that on average these markers will not change in histopathologically normal cells.

To test the robustness of our results to different combinations of neuron markers, we systematically removed each marker and recomputed the GAD results presented in Figure 3.g-h. As seen in Supplementary Figure 4, the choice of neuron markers does not significantly affect the expression changes seen in GAD.

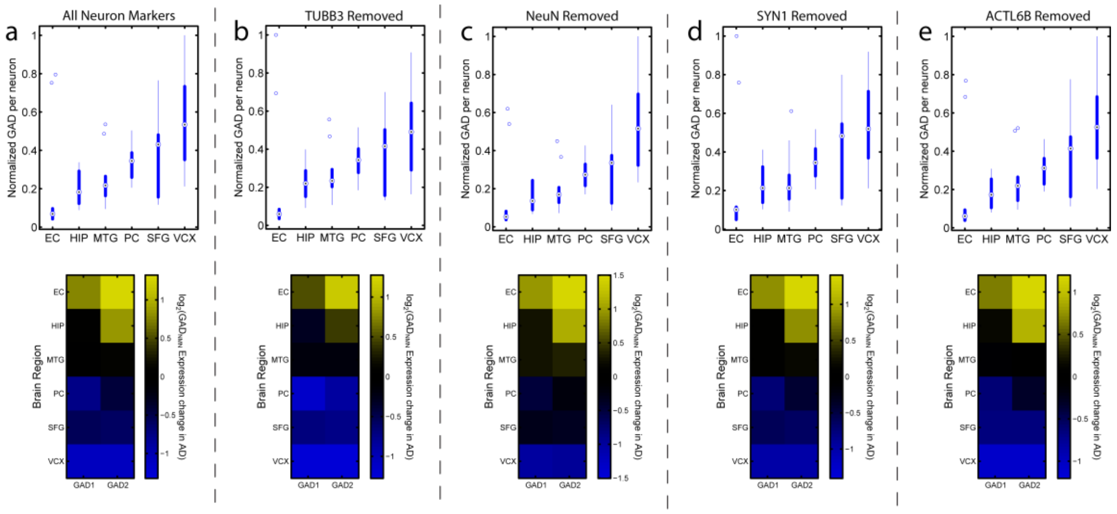

**Supplementary Figure 4. Neuron marker choice has little effect on regional profile of GAD expression.** To test the robustness of the regional profile of GAD expression, each neuron marker used for normalization was removed and the regional profile of GAD expression was assessed. When compared against the profile in which all four neuron markers were used for normalization (a), the results were robust following the removal of (b) TUBB3, (c) NeuN, (d) SYN1, and (e) ACTL6B, thereby demonstrating the robustness of these results.

# *Comparison with previous models of brain energy metabolism*

## General Properties of our models

The reconstruction process detailed in the main text yielded three models containing 1066, 1067, and 1070 compartment-specific enzymatic, transport, and exchange reactions involving 983, 983, and 987 metabolites/compartment combinations, for the glutamatergic, GABAergic, and cholinergic neuron/astrocyte models, respectively. These models accounted for many metabolic processes such as energy metabolism, heme synthesis, quinine biosynthesis, mtDNA turnover, neurotransmitter synthesis and degradation, and biotin metabolism. Complete lists of reactions with the corresponding gene-protein-reaction associations, and citations supporting reaction details are provided in Supplementary Tables 1-4. Additional parameters used to constrain the models are listed in Supplementary Table 5.

## Comparison of pathway inclusion between the previous models and our work

This is not the first time a constraint-based model of brain energy metabolism has been published. Three other manually reconstructed models have been constructed previously [7, 12, 13]. All three contained multiple compartments representing the extracellular space, astrocytes, and neurons. The first of these, the Chatziioannou model, contains 19 reactions with 19 unique metabolite/compartment pairs, and was used to investigate situations in which the glutamate-glutamine cycle was inactive [12]. The second, the Occhipinti model, contains 109 enzymatic and transport reactions, and was used to study the relative pathway activities under different neural activities [13]. The third, the Çakır model, contains 251 reactions/exchanges and 216 metabolites, and was used to investigate the metabolic effects of hypoxic states [7]. Herein we report the first bottom-up reconstruction of a neuron/astrocyte unit in which 1) high-throughput data were used to aid in its construction, 2) associated genes and protein were assigned to reactions, and 3) all reactions were mass and charge balanced.

A brief comparison of each model demonstrates a gradual increase in model scope (see Supplementary Table 8). The Chatziioannou model [12] is a small model encompassing the basic metabolic processes in astrocyte and neuron metabolism in rat. It covers glucose uptake, glycolysis, TCA cycle, the malate-aspartate shuttle, the glutamate-glutamine cycle, etc. Many of the metabolic pathways are compressed into single reactions in this model. The model published by Occhipinti, et al. [13], is of slightly larger scope, including the pathways in the Chatziioannou model, plus oxidative phosphorylation, ketone body metabolism, GABA metabolism, and the phosphocreatine cycle. In this model, many of the metabolic reactions are still lumped into net reactions across several enzymes. The Çakır model [7] covered a much broader range of pathways, especially among amino acid and lipid metabolic pathways. Our models extend the scope of these previous studies. In addition, we have separated lumped reactions, added many additional pathways involving co-factor metabolism (e.g., heme, vitamin D, ubuiquinone, folate, etc.) and the metabolism of a few other carbon sources not included in the other studies. Moreover, we associated genes with each reaction as far as the literature and data allowed (403 genes in total).

## *Gap-filling in the models of brain energy metabolism*

A common property of large-scale metabolic network models is the presence of numerous gaps in the network (see [14] for a review). Gaps can result from various situations. For example, knowledge gaps occur when portions of pathways have not been studied. Scope gaps, on the other hand occur when a metabolite produced in a reaction should subsequently be used in another system in the cell, outside of the scope of the model. For example, in the iAF1260 model of *E. coli* metabolism [15], there are reactions for charging tRNAs. However, translation is currently not addressed in the model, and so there is a scope gap in which the charged tRNAs cannot be used and therefore, the charging reactions cannot carry flux. A review of gap-filling techniques is beyond the scope of this work. However, several reviews and studies have addressed this issue [14, 16-18].

Some gaps are obvious, in which a metabolite in the network can only be produced or consumed. More difficult to address are blocked reactions, which cannot carry a flux because of knowledge gaps, scope gaps, stoichiometric imbalances or the funneling of metabolites into metabolite pools for storage (e.g., lipids in adipocytes). In this work, gaps were addressed as follows. First, all model exchange reactions were opened, allowing the uptake and secretion of all metabolites known to cross the blood brain barrier. Second, flux variability analysis was employed to identify all reactions that cannot carry flux. Reactions from this list were manually inspected. Literature was then used to fill in gaps by either adding reactions that were missing from the models or removing reactions that were not supported by the literature. For example, heme biosynthesis was non-functional in the first draft of the mitochondrial model. However, following a thorough literature search, a few reactions that were outside of the scope of the model were identified and added to complete pathway. This process was continued until most blocked reactions were located in the peripheral regions of the model. Much care was taken to minimize gaps in regions of the models that can affect the novel results presented in this work.

In the end, the fraction of model reactions that were blocked was assessed and compared to other manually curated genome-scale models of eukaryotic metabolism. For this we used the human reconstruction (HR1) and the most recent reconstruction of yeast metabolism, iMM904 [19]. For each model, all metabolite exchanges were opened, allowing the model to uptake and secrete all exchange metabolites. Flux variability analysis was then employed to identify all reactions that cannot carry flux. The percentages of total model reactions that cannot carry flux are shown in Supplementary Figure 5. In this analysis, we found that roughly 34% and 35% of human and yeast reactions were blocked, respectively. The models built in this study, on the other hand had a lower percentage between 25-26%. While these percentages seem high, these models each contain knowledge gaps that are expected to be resolved in future experimental studies, and thereby will be reflected in future versions of these models. This process has been successful for the iAF1260 model of *E. coli* metabolism which now contains fewer than 10% blocked reactions, and many of these blocked reactions are due to scope gaps that will be addressed as the metabolic network is coupled to the transcription and translation machinery [20].

This process of iteratively updating and filling gaps is similar to the process of sequencing genomes, which when first published, usually are not completely sequenced or assembled. Moreover, most genomes have a large number of hypothetical proteins and uncharacterized open reading frames (ORFs). Genomes are subsequently updated over time as the percentage of sequence is increased until completed and the annotation of ORFs and genomic features is continuously updated.

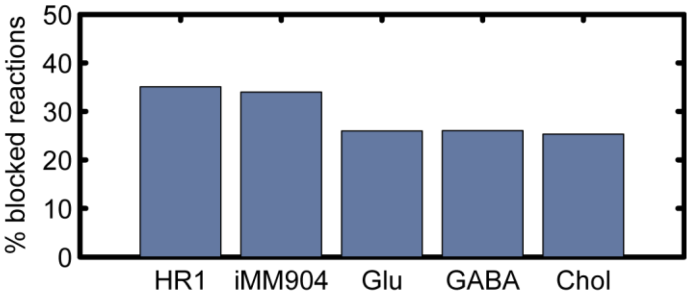

**Supplementary Figure 5. Blocked reactions in large-scale metabolic networks.** A common property of metabolic network reconstructions is the existence of network gaps. These gaps lead to a certain number of reactions that cannot carry flux, even when all exchange fluxes are opened. An aim of the gap-filling process is to minimize the number of blocked reactions. However, limitations in knowledge of metabolism in the given organism and limitations from the model scope lead to a significant portion of model reactions to be blocked. For example, in the human metabolic network (HR1) and the recent yeast metabolic network (iMM904), roughly 35% of reactions are blocked, while the models built for this study have 25-26% of the total reactions, transports and/or exchanges blocked.

## *Previously reported ATP yields are within model predictions*

ATP production and consumption in the human brain can be estimated in several ways (reviewed in [21]). Clark and Sokoloff [22] derive the ATP consumption rate using the assumptions that the 1400g human brain takes up 49ml of $O_2$/min (1.6 µmol/g wet brain/min), that all of the $O_2$ is used for oxidation of carbohydrates, and that the synthesis of phosphate bonds in ATP has an energy conversion efficiency of ~20%. This leads to an ATP consumption rate of 5.1 µmol ATP/g wet brain / min.

Alternatively, since NADH reoxidation in the brain depends mostly on glucose and oxygen, it is assumed that about 2.5 ATP will be produced from each O atom consumed (termed the P/O ratio). Once again we assume a cerebral metabolic rate of $O_2$ of 49ml/min. We must also take into account that about 10% of the oxygen uptake is involved in non-mitochondrial processes and a 20% loss of ATP production potential, due to proton leak (estimated from muscle, heart, and liver [23]). Thus the net rate of ATP consumption is 5.5 µmol ATP/g wet brain / min (see [21] for details).

Here we used the human cerebral metabolic rates for metabolites reported in [5, 6] to compute all feasible net steady state ATP production rates (equivalent to consumption rates at steady state). This was done as follows. First, the models were set up using the cerebral metabolic rates (CMRs) reported by Lying-Tunell, et al. [5, 6], with the reported glucose and $O_2$ CMRs reported by Clark and Sokoloff [22] (used to allow comparison against the reported ATP production rates, which were based on the Clark and Sokoloff values). Second, Monte Carlo Sampling was used to uniformly sample all candidate flux states for the three models presented here, along with the Çakır and HR1 models. To avoid the inclusion of thermodynamically-infeasible loops, a mixed integer linear programming method (ll-sampling) was used to find the nearest loopless flux for each sample point (Schellenberger, et al., submitted). The removal of loops was critical to the remaining steps to avoid the summation of unrealistic production of ATP in these loops. Third, the fluxes of all ATP producing/consuming reactions were normalized by the stoichiometry of ATP in the reaction. Fourth, for each sample point, the sum of all normalized ATP consuming fluxes was subtracted from the sum of all ATP producing fluxes, thereby providing the ATP production rates for each sample point. Lastly, all ATP production rates were multiplied by 0.7 to take into account the 30% loss of ATP production potential from non-mitochondrial usage and proton leak. This resulted in median ATP production rates of 5.7, 5.6, and 5.7 µmol ATP/g wet brain / min for the cholinergic, GABAergic, and glutamatergic models, respectively. These results are within 6-8%, of the published values. While technical issues from the size of HR1 did not allow us to compute its ATP production rate, the Cakir model was tested and returned median ATP production rate of 5.4 µmol ATP/g wet brain / min, which is within 3% of the mean reported value. Thus, our models and the Cakir model were well within the estimated error of the previously reported values, in which it was stated that the true value could be within 25% of the previously reported values [21].

## Models allow for experimentally measured fluxes

In constraint-based modeling, one can constrain the space of feasible metabolic flux distributions by either constraining internal reactions or input/output rates. In this work we used experimentally measured uptake and secretion rates to help constrain the models, also known as cerebral metabolic rates. One challenge in doing this is that it is possible to over-constrain the metabolic network, thereby leading to infeasible solutions because of conflicting metabolite uptake and secretion rates. For example, if one measurement said that between 4-5 units of glucose entered the brain in for a given time frame, and that 36-37 units of $CO_2$ were released, no feasible steady-state solution could be attained since it would require more carbon leaving the brain than would be entering. From the datasets used in this work [5, 6], uptake and secretion ranges for metabolites that are used within the scope of the models did not over-constrain the model, and therefore feasible solutions were attainable.

Predicted internal fluxes are dependent on the uptake and secretion constraints placed on the models. However, it is often difficult to experimentally validate internal fluxes. Many fluxomic studies are able to infer pathway and branch-point fluxes, but can only occasionally infer the flux through a specific enzyme *in vivo*. From the literature, we have identified three enzymes for which reliable *in vivo* fluxes have been determined in the human brain [24-26]. Flux Variability Analysis was used to determine the upper and lower bounds for each of these fluxes in our models, the Çakır model, and the HR1 model, subject to the experimentally-measured cerebral metabolic rates used for all analyses in this study [5, 6]. All experimentally-measured fluxes reside within the solution space of these five models (Supplementary Figure 6).

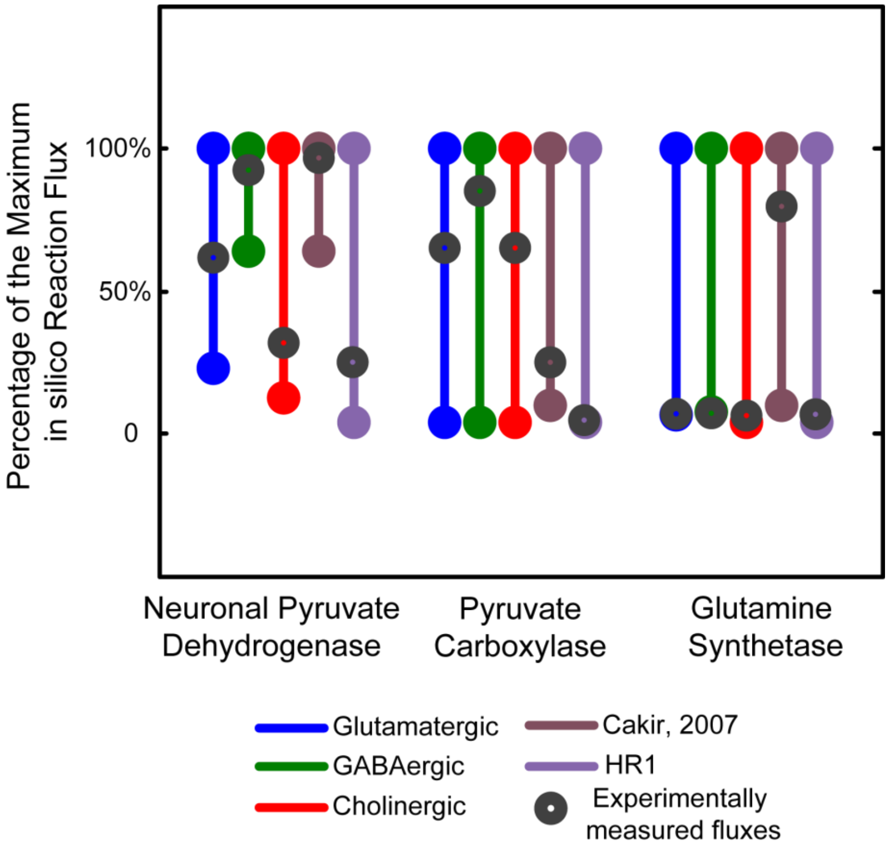

**Supplementary Figure 6. Computed candidate flux states are consistent with experimentally measured fluxes.** Fluxomic experiments have successfully measured several metabolic fluxes in the human brain. A small number of these fluxes were attributable to a specific enzyme in either the neuronal or astrocytic compartments (i.e., neuronal pyruvate dehydrogenase, astrocytic pyruvate carboxylase, and astrocytic glutamine synthetase). These reported fluxes were normalized by the reported glucose cerebral metabolic rates (CMR) so that the CMR would be consistent with the rates used in our models. The rates were then compared to the ranges of feasible metabolic fluxes in our models, the Çakır model and the HR1 model, with the upper and lower bounds for each model denoted by the round ends. All fluxes were scaled by the maximum feasible flux for the respective enzyme for each model to allow for improved visualization. All experimentally-measured fluxes reside within the solution spaces of the five models.

## *Model predicts that GABAergic neurons are the primary users of the GABA shunt*

Most, if not all neurons, have enzymes that contribute to a bypass in the TCA cycle called the GABA shunt; however, it has been reported to be predominant in GABAergic cells [27]. This shunt routes flux from α-ketoglutarate to succinate. *In vitro* estimates suggest that this pathway may normally account for between 1/10 and 1/3 of the brain TCA cycle flux [27, 28]. In mouse GABAergic neurons, the flux through the GABA shunt is about the same as flux through AKGDm [27], suggesting that a majority of GABA shunt activity is found in GABAergic cells. In our simulations, GABAergic neurons are consistent with these results, showing a slightly lower feasible flux range for the GABA shunt than seen for AKGDm, while cholinergic and glutamatergic neurons show a very small flux through the GABA shunt enzymes (see Supplementary Figure 7).

The small flux in cholinergic and glutamatergic neurons is due to the degradation of neurotransmitter that is available from outside of the neurons. *In vivo*, there is also a small amount available as non-GABAergic neurons break down GABA released from GABAergic neurons. Thus our simulations suggest that a distinction should be made in the naming of the GABA shunt in the different neuron types, since the GABA shunt is not a true shunt in non-glutamate decarboxylase-expressing neurons. In these neurons the other GABA shunt enzymes primarily plays a role of a degradation pathway with no replenishment within the same cell.

When this analysis is done on other models, the Çakır model shows that the brain has the same flux range for the two pathways, while the HR1 model GABA shunt flux is less than 2% of the TCA cycle flux. Both of these are outside of the 1/10-1/3 ratio of GABA shunt to TCA cycle flux reported previously, primarily because neither model was designed to encapsulate neuron-type specific responses.

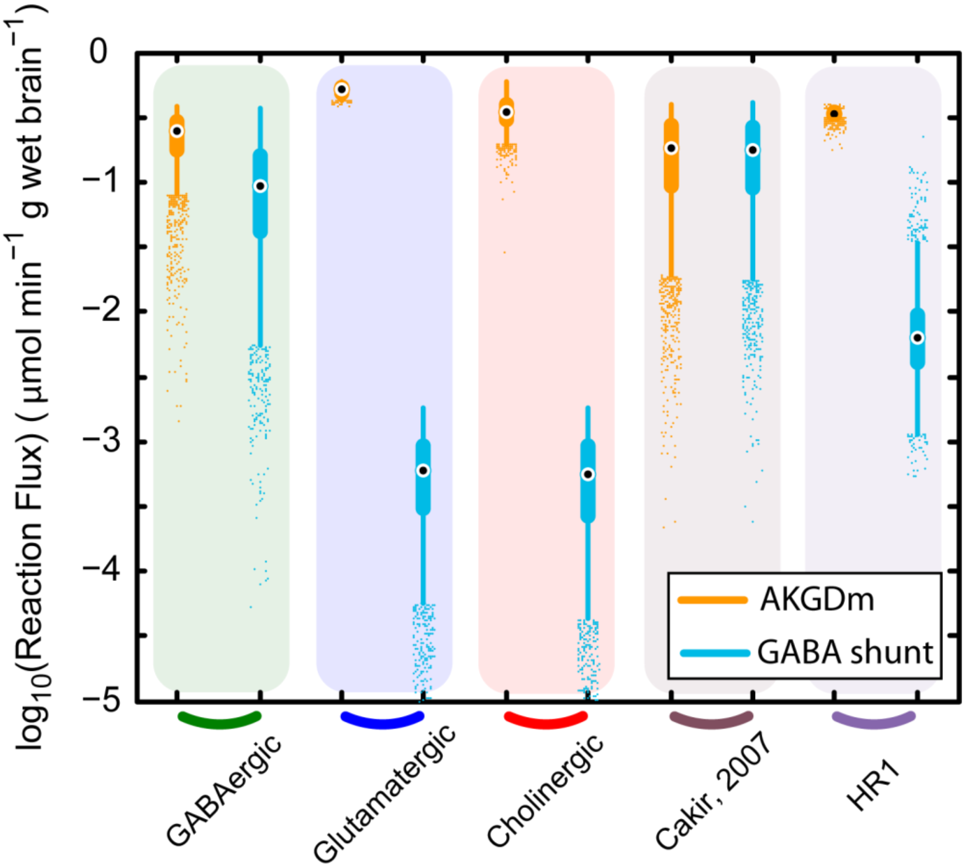

**Supplementary Figure 7.** ***In silico*** **GABA shunt usage in different neuron types is consistent with the reported** ***in vivo*** **usage.** While most neurons have active GABA shunt enzymes, the level of shunt activity is neuron-type specific. *In silico*, glutamatergic and cholinergic neurons carry a flux through GABA shunt enzymes. However, the activity of the shunt negligible, i.e., orders of magnitude lower than the flux through the TCA cycle. However, the distribution of feasible flux states for the GABA shunt in GABAergic neurons is similar to the flux through the TCA cycle. The Çakır model and entire HR1 model are also shown for comparison. Box plots show the distributions of 5000 samples.

## *Altered correlation between reactions in different neuron types can be used to systematically identify underlying mechanisms of neuron-type specific effects*

In these models, the flux through each reaction can have complete, strong, moderate, or no dependency on the flux through other reactions in the model [29]. These can also be described as “reaction correlations” in which a Pearson’s correlation coefficient is computed for the flux values for two reactions, using all sampled feasible flux states. For each model, reaction correlation coefficients were computed for all possible reaction pairs and compared between the three neuron types. Differences in the model topologies lead to significant changes in a small subset of reaction pair dependencies, as seen by the off-diagonal points in Supplementary Figures 8.a-c. Many of these are of little interest, since many belong to pathways that process the different neurotransmitters. However, a small number are of great interest, showing unexpected differences between neuron types. One of particular interest is the reaction correlation between neuronal α-ketoglutarate dehydrogenase and oxidative phosphorylation. In glutamatergic and cholinergic neurons, these reactions are tightly coupled. However, in GABAergic neurons, these reactions are decoupled (Supplementary Figure 8.d), providing additional support that the metabolic network topology should lead to cell-type specific responses in Alzheimer's disease or thiamine deficiencies, which affect α -ketoglutarate dehydrogenase [30]. The correlation coefficient for the Çakır and HR1 models, also demonstrated a correlation near zero, demonstrating that the analysis of cell-type specific networks can provide addition insight that cannot be attained using more coarse-grained models.

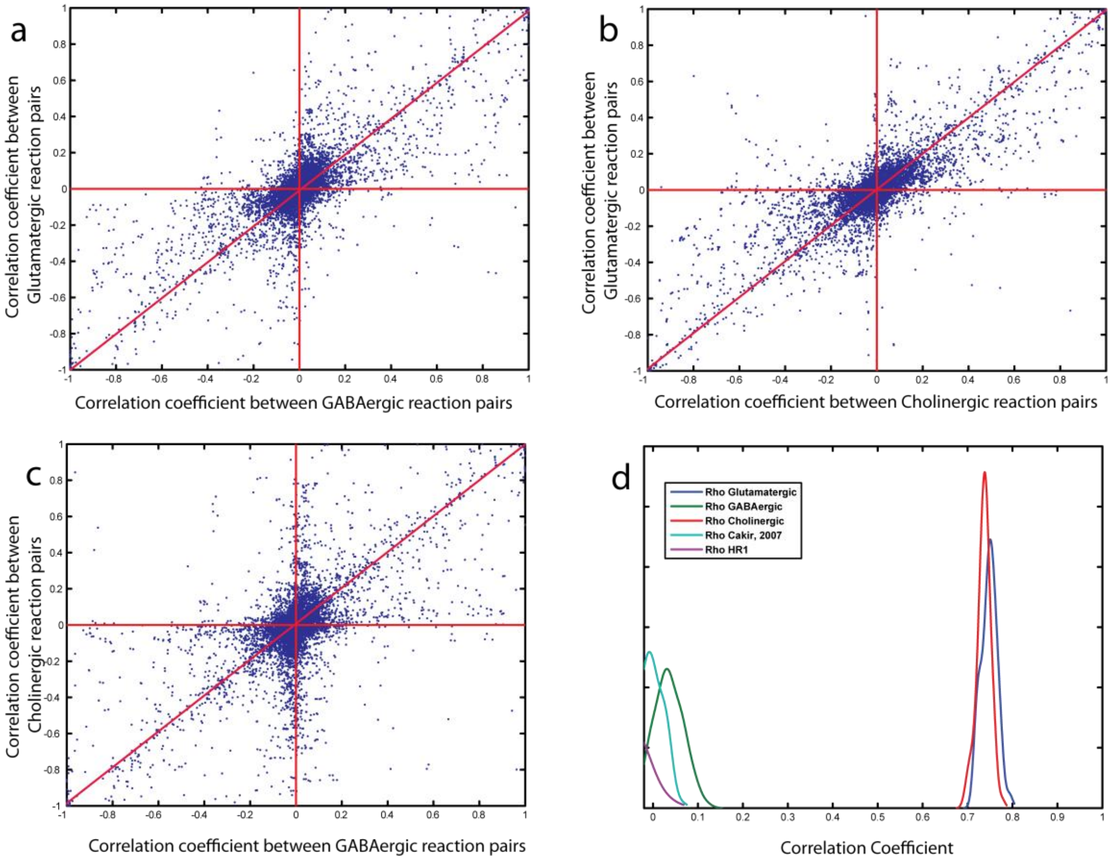

**Supplementary Figure 8. Cell-type-specific co-dependencies can be queried to identify cell-type-specific responses under cellular perturbation.** The correlation between reaction fluxes within reaction pairs is computed, and repeated for each model. It is expected that if two models are similar as in the cases of the different neuron-type models, most reaction pairs will have similar reaction pair correlation coefficients (i.e., will lay near the bold red diagonal in (a)-(c)). However, reactions that are distant from the diagonal demonstrate inherent differences between the cell types. When this is computed for the three neuron models, only a small fraction of conserved reaction pairs have significantly different reaction-pair-correlations (a)-(c). For example, (d) the bootstrapped correlation between neuronal α-ketoglutarate dehydrogenase and cytochrome c oxidase is near zero in GABAergic neurons, but ~0.75 for glutamatergic and cholinergic neurons, demonstrating the susceptibility of these neuron types to alterations in α-ketoglutarate dehydrogenase activity.

## *An assessment of correlated reaction fluxes computed using Monte Carlo sampling and other methods*

The method presented above can be successfully employed to predict target reactions, for which perturbations may lead to cell-type-specific effects. However, the question remains about how it performs compared to other published methods such as the Flux Coupling Finder [31] and Hard-Coupled Reaction sets [32].

In this study, we utilized Monte Carlo random sampling to determine potential flux states in the solution space. By comparing the individual fluxes against one another, we were able to calculate the correlation coefficients. Highly correlated reactions were deemed to be coupled. In addition, reaction pairs with a correlation coefficient of 1 or -1 were deemed perfectly correlated.

Other approaches to determine coupled fluxes include the Hard-Coupled Reaction (HCR) sets [32] and Flux Coupling Finder (FCF) [31] methods. The HCR method involves looking only at the stoichiometry of the network. The method is unbiased since flux constraints are ignored and only perfectly correlated reactions are calculated. On the other hand, FCF iteratively fixes a flux in the network and calculates the accompanying changes through optimization of the other fluxes. If a flux is then fixed or changed, the pair is deemed fully or partially coupled, respectively. However, the model has to be first converted into an irreversible model, thereby increasing the size of the network. Here, we compared the three methods for the glutamatergic neuron model, though results are qualitatively similar for any of the three models presented in this work.

HCR sets were calculated for the glutamatergic neuron model (Supplementary Table 12). When comparing the HCR method with the other methods, we removed all reactions that could not carry a flux in the glutamatergic neuron model. This was done to ensure a direct comparison because the other two methods cannot pick up coupled reactions between reactions with no fluxes. All HCR sets were detected by the sampling method as perfectly correlated (R = 1 or -1). However, not all perfectly correlated reactions from the sampling method were detected by HCR calculation. The flux constraints during sampling provide an additional means of coupling reactions, thereby allowing the identification of coupled reaction sets beyond the stoichiometrically coupled reaction sets from the HCR method.

Supplementary Table 12. A comparison between different methods used for assessing coupled reaction sets.

| | HCR | FCF (fully coupled) | FCF (partially coupled) | Sampling (perfect correlation) |
|---|---|---|---|---|
| Number of Sets | 232 | 80 | 83 | 340 |
| Average Length | 2.99 | 2.8875 | 2.96 | 2.17 |
| Max Length | 14 | 7 | 11 | 19 |
| Min Length | 2 | 2 | 2 | 2 |

We subsequently compared the sampling method to FCF. FCF returns sets of reactions that are fully, partially or directionally coupled. The fully coupled reactions were similar to the hard coupled sets and the perfectly correlated reactions calculated from randomized sampling (Supplementary Table 12). In fact, all 80 fully coupled sets from FCF had perfect correlations (R = 1 or -1) in the sampling data. It was interesting to see that even though the sampling method had a higher maximum set size, the average set size was smaller due to more numerous small sets in the sampling results.

Looking at the partially coupled sets, there were some surprisingly results. There were 82 different sets that corresponded to 173 reaction pairs that were partially coupled. To compare the FCF and sampling methods, we determined the correlation coefficients of the 173 pairs. 30 pairs had perfect correlation (R = 1 or -1) while 58 had correlation coefficients with p values greater than 0.05. Unlike the HCR and FCF (fully coupled) results, the partially coupled results were not fully in agreement with the sampling method. We believe there are two main reasons. First, most reaction sets that were perfectly correlated from sampling were originally reversible and were split into irreversible forward and reverse reactions. The perfect correlation could be the result of using an irreversible model where one direction is dominant and perfectly correlated while the other is not. Second, uncorrelated reactions can be labeled as partially coupled in FCF if fixing a flux using FCF results in even a small change in flux. No statistical measure limits the sensitivity of this coupling for certain reactions, and thus insignificant pairs can be reported in FCF.

However, overall there is good agreement between the HCR, FCF (fully coupled) and the perfectly correlated sampling results. The co-sets from the HCR and FCF (fully coupled) were also reported by the sampling method, as well as some additional co-sets that the other methods did not pick up. Partially coupled results were not in as good agreement with the sampling method because of the use of an irreversible model for FCF, as well as the two methods using much different criteria for correlation.

## *Identifying genes that decouple α-ketoglutarate dehydrogenase from oxidative phosphorylation*

As seen in Figure 3 in the main text and Supplementary Figure 8.d, cholinergic and glutamatergic neurons demonstrate a significant coupling between α-ketoglutarate dehydrogenase (AKGDm) and oxidative phosphorylation (OxPhos). However, GABAergic neurons do not show this property. What causes these neuron-type-specific responses that correspond to the pattern of neuron-type sensitivity in AD? To identify potential targets that lead to this decoupling of AKGDm to OxPhos, each reaction in the GABAergic model was systematically removed, followed by Monte Carlo sampling of the modified model and computation of the AKGDm and OxPhos correlation. From this, a handful of neuronal reactions, upon removal, significantly couple AKGDm to OxPhos, including atp synthase, various glutamate and GABA transporters, and glutamate decarboxylase. The reverse computation was done in which each of the coupling reactions were systematically added to the glutamatergic model (if not in the model) followed by Monte Carlo sampling of the modified model and computation of the AKGDm and OxPhos correlation. From this analysis, only one reaction decoupled AKGDm and OxPhos. This reaction (GLUDC_Neuron) is catalyzed by glutamate decarboxylase, which is encoded by either of two isoforms of the GAD gene.

## *Regional specificity of differentially expressed pathways in Alzheimer's Disease using PathWave*

We performed the systematic pattern recognition method PathWave [33] (with 10,000 permutations) on the three models by mapping the gene expression data, obtained from the Gene Expression Omnibus (GSE5281), on the corresponding reactions. This resulted in 63,352 features for each model. The p-value for each pathway was corrected for multiple testing (FDR = 0.05) [34]. Only pathways with more than three significantly differentially regulated reactions (FDR = 0.05) were further considered. This allowed us to focus on the most relevant wavelet features. Each brain region demonstrated a slightly different subset of differentially expressed pathways and underlying reactions. The perturbed pathways and reactions for each brain region can be found in Supplementary Table 11, but are also discussed here.

**Visual cortex (VC) and Superior frontal gyrus (SFG):** No significant patterns were identified in these regions. This is consistent with previously reported results that these regions show little change metabolically in Alzheimer's disease when compared to age-matched controls [11].

**Entorhinal cortex (EC):** Nine pathways were identified to carry a pattern of significantly changed regulation in AD. All 48 differentially regulated reactions were down-regulated. As noted in the main text, central energy metabolism (i.e., TCA cycle, Glycolysis, and the pentose phosphate pathway) was down-regulated, consistent with the decreased metabolic rate reported previously [35]. However, the most significantly changed pathway was the ethanol and acetate metabolism. Ethanol monooxygenase and alcohol dehydrogenase, both responsible for the metabolism of ethanol, were down-regulated. It is possible that this lower expression of ethanol-catabolizing genes in Alzheimer's patients could be serving a neuroprotective function for the remaining cells by causing small increases in the brain ethanol concentration, since it has been previously shown that moderate increases in ethanol concentration in brain increases the expression of heat shock protein 70, which may protect against oxidative stress and glutamate excitotoxicity common in Alzheimer's disease [36]. However, this suggestion is just speculation because the effect of ethanol on AD brain is still poorly understood. Current literature, while supporting the idea that low levels of alcohol consumption may decrease the progression of cognitive impairment [37], also suggests that larger amounts of alcohol increase the incidence of Alzheimer's disease [38]. However, it is unclear if these effects are affected by lifestyles that are associated with different levels of drinking [39], or even by misclassification of participants, as seen with studies on alcohol and coronary health [40]. More work is needed to investigate this suppression of ethanol-catabolizing genes in AD.

**Hippocampus (HIP):** Nine pathways showed significant patterns consisting of 53 down-regulated reactions. The down-regulation of reactions of the TCA-cycle, malate-aspartate shuttle, and glycolysis is consistent with the decreased metabolic rate reported previously [35].

Interestingly, a couple other pathways were significantly suppressed, although the individual reactions therein were only weakly differentially regulated ($p < 0.05$, but higher than the FDR cutoff). Oxidative phosphorylation was weakly down-regulated, while ROS detoxification (catalase and glutathione oxidoreductase) was weakly up-regulated in AD to cope with increased oxidative stress [38, 41] (except for a significant down-regulation of superoxide dismutase; $p = 0.0009$).

**Posterior cingulate cortex (PC):** In total, 19 significantly regulated pathways were identified in the PC having in total 151 down-regulated and 2 up-regulated reactions. Central energy metabolism (the TCA cycle, glycolysis, the malate-aspartate shuttle, oxidative phosphorylation, and glyoxylate metabolism) were all down-regulated [42], consistent with the finding that metabolism in this region is decreased more than expected from atrophy [35]. In addition, there was significant down-regulation of the transport and degradation of various amino acids, such as glutamate, cysteine, alanine (through alanine-glyoxylate transaminase), lysine, and a decreased expression of the glycine-cleavage complex.

**Middle temporal gyrus (MTG):** The middle temporal gyrus has 18 differentially regulated pathways with 102 down-regulated and 13 up-regulated reactions. Consistent with the other affected brain regions, there is significant suppression of central metabolism (i.e., the TCA cycle, glycolysis, the malate-aspartate shuttle, and oxidative phosphorylation). For heme biosynthesis, protoporphyrinogen oxidase, uroporphyrinogen-III synthase, uroporphyrinogen decarboxylase, and mitochondrial ferrochelase were down-regulated ($p < 0.0009$) which suggests that there may be decreased heme production. Since heme is important for cytochrome c oxidase function, it has been previously suggested that a disruption in the pools of different hemes may contribute to the pathology of Alzheimer's disease [43]. Thus, the bioenergetics of this region may be suppressed due to a decreased cytochrome c oxidase function from a decreased biosynthetic capacity of heme.

## *Identifying feasible pathways which can couple acetylcholine production to mitochondrial acetyl-CoA*

Metabolism is arguably one of the best characterized biomolecular systems in human. However, a recently published neurochemistry textbook states, "The acetyl-CoA used for acetylcholine synthesis in mammalian brain comes from pyruvate formed from glucose. It is unclear how the acetyl-CoA, generally thought to be formed at the inner membrane of the mitochondria, accesses the cytoplasmic choline acetyltransferase (ChAT)" [22]. It has been clearly demonstrated in numerous studies that the acetyl group of mammalian neuronal acetylcholine is derived from the mitochondrial acetyl-CoA pool [44, 45], and that acetylcholine production is dependent on oxidative metabolism [46]. However, it is surprising that something as simple as how the acety-CoA in the mitochondria can contribute to cytosolic acetylcholine production has eluded discovery for decades. A few pathways have been proposed, but several questions still remain [47].

This connection is of great interest since it has been shown that the tight coupling of metabolism with acetylcholine production facilitates treatments that increase glucose uptake in the brain to improve cognitive functions in rats [48-50] and humans with severe cognitive pathologies, such as Alzheimer's Disease and Trisomy-21 [51, 52].

As discussed in the main text and methods, an FBA-derived approach was employed to identify all possible pathways using known reactions in the human metabolic network. The Singular Value Decomposition of all possible reaction sets helped elucidate the dominant sets of reactions, and their major dependencies, that could be used to couple mitochondrial acetyl-CoA metabolism and cytosolic acetylcholine metabolism. The first singular vector provided information on the number of times a reaction was used for a pathway, i.e., reactions with large loadings were found in many pathways. The second and third singular vectors, however, show groups of reactions that occur more often together or less frequently. Visual inspection of these vectors helped elucidate 3 potential mechanisms. Predicted pathways seen in the second and third singular vectors include the following:

1. Acetate can form acetyl-CoA through acetyl-CoA synthetase (ACS) (Figure 5.a). However, this is enzyme is cytosolic. Therefore, to couple mitochondrial acetyl-CoA and cytosolic acetate, a series of additional enzymes are needed. This can be done using aspartate N-acetyltransferase (ASPNATm) to make N-acetyl-L-apartate, which is then transported across the mitochondrial membrane (NACASPtm), and hydrolyzed by N-acetyl-L-aspartate amidohydrolase (NACASPAH). Several malate-aspartate shuttle enzymes are further needed for this pathway to shuttle the aspartate back to the mitochondrion (e.g., ASPGLUm and GLUt2m). The only problems with this mechanism are that several of the enzymes show little or no neuronal expression. High-throughput data and the literature demonstrate that cytosolic acetyl-CoA synthetase is not active in neurons [53]. Also, N-acetyl-L-aspartate amidohydrolase is not significantly expressed neurons, rather in oligodendrocytes [54] for myelin sheath production. Therefore it is unlikely that this pathway is contributing to the mitochondria/acetylcholine coupling.

2. Acetyl-CoA can be incorporated into the citric acid cycle by citrate synthase (CSm) to form citrate (Figure 5.b). This citrate is then shuttled to the cytosol through a citrate-malate antitransporter (CITtam). Once in the cytosol, the acetyl-CoA can be produced by citrate lyase or ATP citrate lyase [55] (ACITL). The malate-aspartate shuttle is also used to replenish the cytosolic malate pool (AKGMALtm, ASPTAm, ASPTA, and ASPGLUm). Several studies have suggested that that ACITL might be of physiological importance in linking mitochondrial acetyl-CoA with cytosolic acetylcholine synthesis, with experimental evidence such as isotope-labeling experiments [45] and co-localization of choline acetyltransferase with citrate lyase [56]. However, its importance has been questioned when a study demonstrated that when citrate lyase is inhibited by (-)-hydroxycitrate, the synthesis rate of acetylcholine from glucose or pyruvate decreased to only ~70% of control [57].

3. A third possible pathway involves mitochondrial ketone body synthesis (Figure 5.c). Mitochondrial acetyl-CoA can be converted into acetoacetate by mitochondrial acetyl-CoA C-acetyltransferase and 3-oxoacid CoA-transferase (ACACT1rm and OCOAT1m), which can then be transported into the cytosol (ACACt2m) and

converted to acetoacetyl-CoA by acetoacetyl-CoA:acetate CoA-transferase (AACOAT) and then to acetyl-CoA by acetyl-CoA C-acetyltransferase (ACACT1r) [58, 59]. It is plausible that this pathway is used since it has been reported that ketone bodies, such as beta-hydroxybutyrate [60] and acetoacetate [61], can act as precursors to the acetyl moiety of acetylcholine.

While this analysis helped guide manual curation for these pathways, a thorough literature search identified a fourth potential pathway, which was not seen in the SVD results. It has been suggested that acetyl-CoA can be produced from acetyl carnitine via cytosolic carnitine acetyl transferase (CSNATr). This has also been investigated experimentally and evidence has been presented that in the cytosol, labeled acetylcarnitine can produce labeled acetylcholine in both brain slices and synaptosomes [62, 63]; however, these studies did not demonstrate that the acetylcarnitine associated with the mitochondrial metabolism, since the tissue samples were only incubated in acetylcarnitine [63]. Moreover, the labeled neurotransmitter yield was low, except when the synaptosomes were incubated in higher concentrations of acetylcarnitine. Therefore, this pathway is likely of little importance in the brain [47]. It should also be mentioned that such a mechanism would require the carnitine shuttle to run in reverse by passing acetyl carnitine from the mitochondria to the cytosol [64], and therefore cannot explain the coupling of mitochondrial metabolism to cytosolic acetylcholine production. Therefore, this pathway was not analyzed further.

Pathways 2 and 3 are best supported by the literature and by the high-throughput data. However, pathway 1 could not be made functional in our models without the addition of reactions that are known not to be found in neurons. When pathways 2 and 3 were tested separately and together, they are functional and will produce acetylcholine. When tested separately, both the fluxes of both correlate significantly with the choline acetyltransferase flux ($p < 3 \times 10^{-90}$); however, pathway 2 is only weakly correlated ($r = 0.28$), while pathway 3 is more strongly correlated ($r = 0.81$). Consistent with experimental inhibition of (ACITL), the *in silico* inhibition of ACITL only partially reduces acetylcholine production (by 7.3%). However, the inhibition of pathway 3 reduces acetylcholine production by 39%. *In vivo* perturbation of these pathways should cause more significant changes than the *in silico* simulations, since in the models, if one pathway is inhibited, the other can immediately increase flux as needed, but *in vivo*, transcriptional regulatory programs would need to change. Therefore, these results are consistent with experimental results that have shown that when ACITL is inhibited, acetylcholine production continues at 70% of the WT rate [57].

## *Predicting cholinergic neurotransmission*

The work of Gibson et al. [45] has provided experimental data that, in theory, can be used to predict the contribution of cholinergic neurotransmission to total brain activity. In this study, rat brain minces were incubated in solutions that contained [1-$^{14}$C]-pyruvate or [2-$^{14}$C]-pyruvate. Acetylcholine and radio-labeled $CO_2$ were subsequently measured. Several pyruvate dehydrogenase inhibitors were used to demonstrate that when pyruvate dehydrogenase was inhibited, acetylcholine production was also suppressed.

With the model, simulations were conducted in which the brain was allowed a specified range of pyruvate (covering the range seen from [45]). Using Monte Carlo sampling, all functional metabolic states were computed for a normal brain, and then for several levels of inhibition of pyruvate dehydrogenase. The simulations successfully reproduced the linear relationship between acetylcholine production and metabolic rate seen experimentally, and acetylcholine production was correlated with $CO_2$ release (r=0.68). However, the predicted acetylcholine production was too high. This was expected since the model assumes that all neurons in the brain are cholinergic, while the actual amount is not known. If this percentage were known, it could simply used to scale cholinergic-specific reactions (such as choline acetyltransferase).

The percentage cholinergic neurotransmission was computed based on published data [45]. The previously published data were obtained from rat brain minces that were incubated in solutions containing [1-$^{14}$C]-pyruvate or [2-$^{14}$C]-pyruvate. Both acetylcholine and radio-labeled $CO_2$ were measured at various titrations of several different inhibitors of pyruvate dehydrogenase. Inhibitors were as follow: 2-oxybutyrate, bromopyruvate, pentobarbital, 2-oxo-4-methylpentanoate, 2-oxobutyrate, amobarbital, 2-oxo-3-methylpentanoic acid, leucine, and 2-oxo-3-methylbutanoate. Based on network structure, most of the radio-labeled carbon from [1-$^{14}$C]pyruvate will be converted to radio-labeled $CO_2$ from pyruvate dehydrogenase and TCA cycle enzymes (via pyruvate carboxylase). However, the bulk of radio-labeled carbon from the [2-$^{14}$C]pyruvate will be converted to radio-labeled $CO_2$ in the TCA cycle, though a portion of the radio-labeled carbon will be sequestered through biosynthetic pathways that siphon off TCA cycle intermediates.

Simulations were conducted using the cholinergic model. The models were allowed to take up the same substrates provided experimentally [45], at rates consistent with the data. Monte Carlo sampling was used to identify all feasible flux states. This was done for various levels of pyruvate dehydrogenase inhibition ranging from 0 to 90% inhibition. The percentage cholinergic neurotransmission was computed by randomly selecting a feasible flux state from each level of pyruvate dehydrogenase inhibition and computing the slope of between choline acetyltransferase and radio-labeled $CO_2$–producing reactions. For [1-$^{14}$]-$CO_2$, the $CO_2$ producing reactions included neuronal and astrocytic pyruvate dehydrogenase. In addition, the flux of astrocytic pyruvate carboxylase was also taken into account since it can incorporate the labeled $CO_2$, which would be later lost through isocitrate dehydrogenase. Specifically, this was computed as follows:

$$\text{labeled } CO_2 \text{ produced} = \text{PDHm\_Neuron} + \text{PDHm} + \text{PCm},$$

where PDHm_Neuron and PDHm are the fluxes through the neuronal and astrocytic pyruvate dehydrogenase, respectively, and PCm is the flux through astrocytic pyruvate carboxylase.

For [2-$^{14}$]-$CO_2$, the labeled $CO_2$-producing reactions are astrocytic and neuronal isocitrate dehydrogenase and α-ketoglutarate. However, since labeled carbon can also be sequestered in other products, the amount of $CO_2$ was adjusted to account also for the amount of labeled carbon expected to be sequestered in acetate, glutamate and glutamine. Specifically, this was computed as follows:

$$\text{labeled } CO_2 \text{ produced} = (\text{ICDHxm} + \text{ICDHxm\_Neuron} + \text{ICDHyrm} + \text{ICDHyrm\_Neuron} + \text{AKGDm} + \text{AKGDm\_Neuron} - 2 * \text{EX\_ac(e)} - 3 * \text{EX\_gln-L(e)} - 3 * \text{EX\_glu-L(e)}) / 2$$

where ICDHxm_Neuron, ICDHyrm_Neuron, ICDHxm, and ICDHyrm are isoforms of neuronal and astrocytic isocitrate dehydrogenase, AKGDm and AKGDm_Neuron are astrocytic and neuronal α-ketoglutarate dehydrogenase, and EX_ac(e), EX_gln-L(e), and EX_glu-L(e) represent the efflux of acetate, glutamine and glutamate from the brain.

A similar slope of acetylcholine production vs. labeled $CO_2$ production was generated from random points sampled from the reported experimental distributions. The ratio of the experimental and *in silico* slopes represents a feasible percentage cholinergic neurotransmission. This was repeated 1000 times, yielding the distributions in Supplementary Figure 9 and a median value of 3.3%. This amount is lower than the experimentally determined percentage of cholinergic neurons in the rat basal forebrain, where it was determined that neurons with choline acetyltransferease make up ~6% of the neurons [65]; however, this higher percentage is of no surprise since the basal forebrain is a major center of cholinergic neurons, and functions in which the basal forebrain participates (e.g., attention, learning, and memory) depend on cholinergic processes.

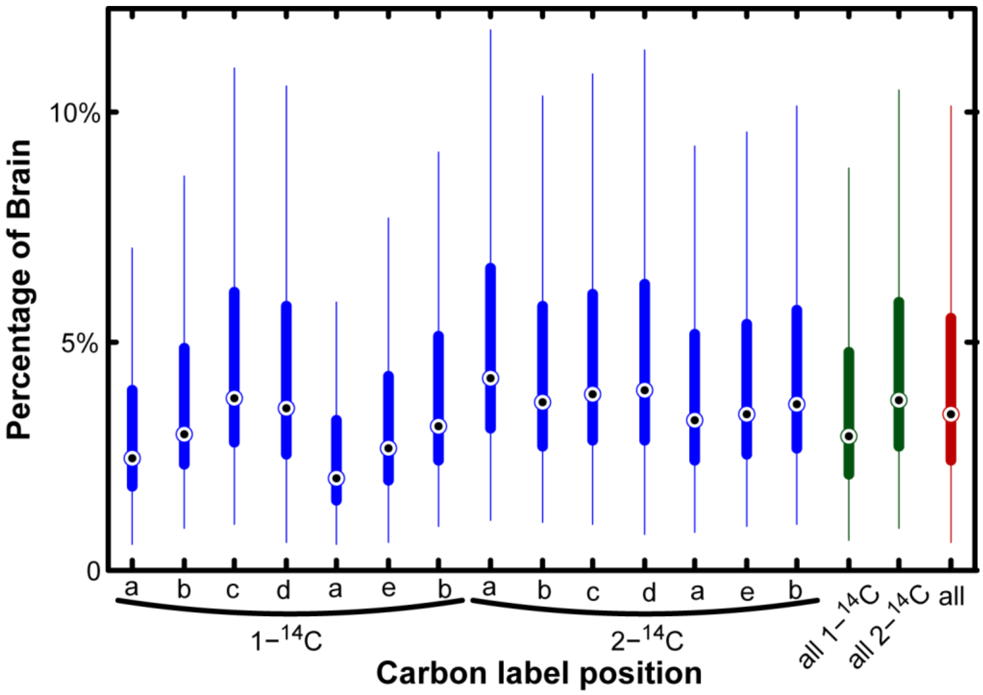

**Supplementary Figure 9. Percentage of brain neurotransmission associated with cholinergic function as predicted from reconciliation of model with each experimental data set.** Fourteen sets of experimental data in which brain minces were fed $^{14}$C-labelled pyruvate, followed by the measurement of $^{14}$C-labeled $CO_2$ and/or acetylcholine were compared with model predictions. For each experiment (blue), a distribution of computed percent brain fractions is shown, representing the range of feasible amounts of the brain that can generate the response seen in the experimental data. Data results for all calculations conducted with [1-$^{14}$C]-pyruvate and [2-$^{14}$C]-pyruvate data (green) show a slight difference; however, the median values are well within the 25th and 75th percentiles (boxes). Individual drug treatments which allow for the computation are as follow: a) 2-oxybutarate, b) bromopyruvate, c) pentobarbital, d) 2-oxo-4-methylpentanoate, and e) amobarbital.

## *Parameter usage from rat brain*

In this work, a few model parameters were used based on rat data when comparable human data was not attainable. These two parameters are the ratio of neuronal to astrocytic glucose uptake rates, and the ratio of glutamatergic to GABAergic neurons (Supplementary Table 5).

For the cell-type-specific glucose uptake rate, data was obtained from a study that used a fluorometric assay to measure the difference between the astrocytic and neuronal glucose uptake rates [66]. Unfortunately, no similar measurements for human are attainable at this time. This is only a concern because rats have a higher neuron:astrocyte ratio. This ratio is 0.7:1 in human and 2.5:1 in rat brain [67]. However, there is no literature that compares the difference in the metabolic rates of the neurons and astrocytes in human. Therefore, the neuron:astrocyte ratios can be extrapolated to the glucose metabolic rates of the different cell populations in rat. This was implemented, and neuronal effects of the AKGDm inhibition presented in Figure 3 of the main text were recomputed. When this is done, the same results presented in the main text are attained (Supplementary Figure 10). Because there is no solid evidence that the differences in the neuron:astrocyte ratio are also reflected in the metabolic rates of these cell populations, we have retained the rat values in the model.

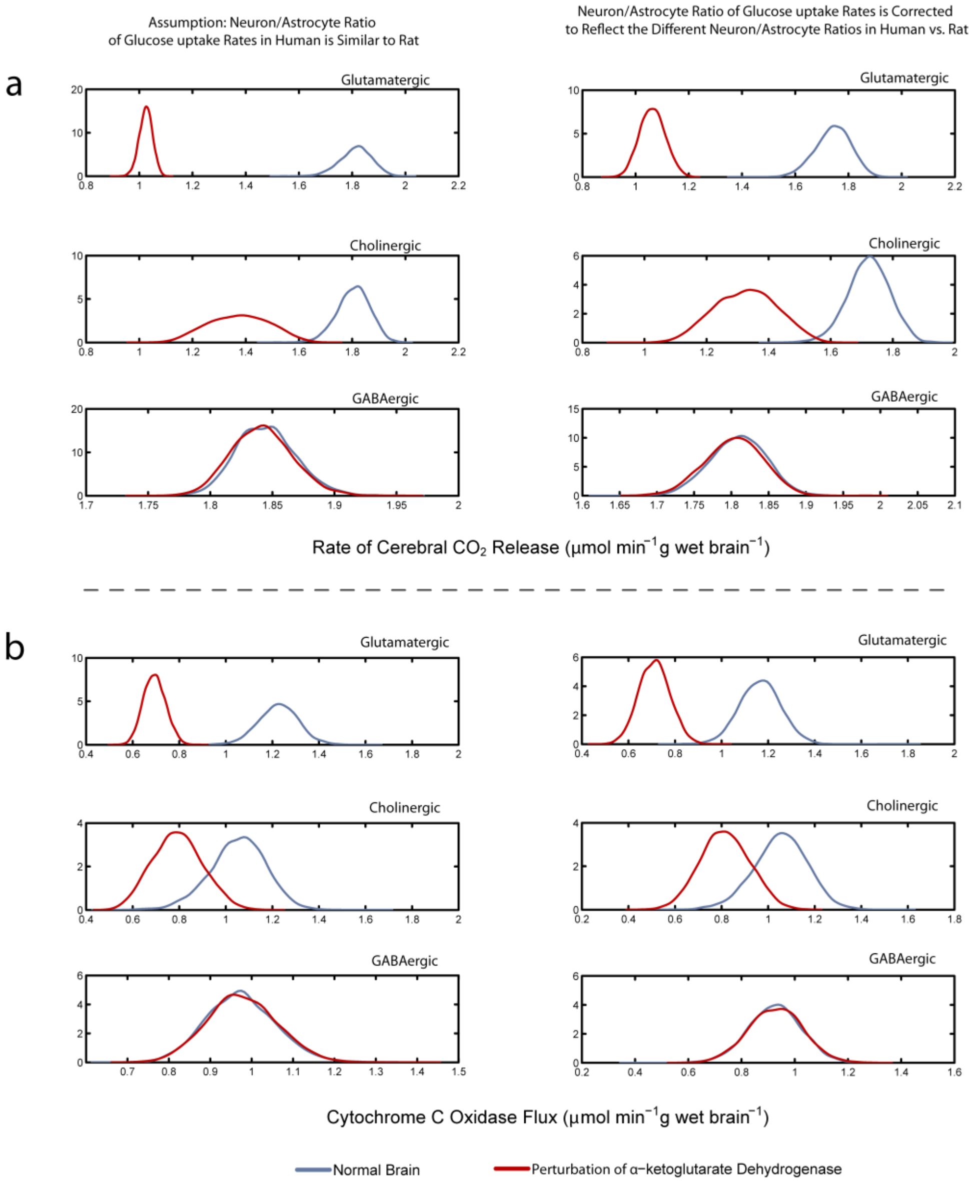

**Supplementary Figure 10. Results in this work are not affected by adjusting the rat Neuron/Astrocyte glucose uptake rate ratio to reflect the difference in the Neuron/Astrocyte ratio in human vs. rat.** When the glucose uptake rates for the different cell populations in the models were adjusted to account for the difference in cell population ratios between human and rat, the results are essentially the same as if the ratios from rat brain are used for both (a) the rate of cerebral $CO_2$ release and (b) flux through oxidative phosphorylation.

A second parameter was derived that allowed the imposition of lower bound on the release of GABA and glutamate from the neurons into the synapses. These bounds were derived using the human rate of glutamate cycling in the brain and the ratio of the number of glutamatergic to GABAergic neurons in rat. However, this parameter is only relevant to the analysis of the loss of AKGDm activity in Alzheimer's disease brain in the main text. Therefore, the glutamatergic/GABAergic neuron ratio was varied from 5/1 to 0.8/1 (rat is 3/1) and the AKGDm inhibition analysis was redone (Supplementary Figure 11). Again, the only analysis in the main text that might be affected by this parameter was robust against its variation.

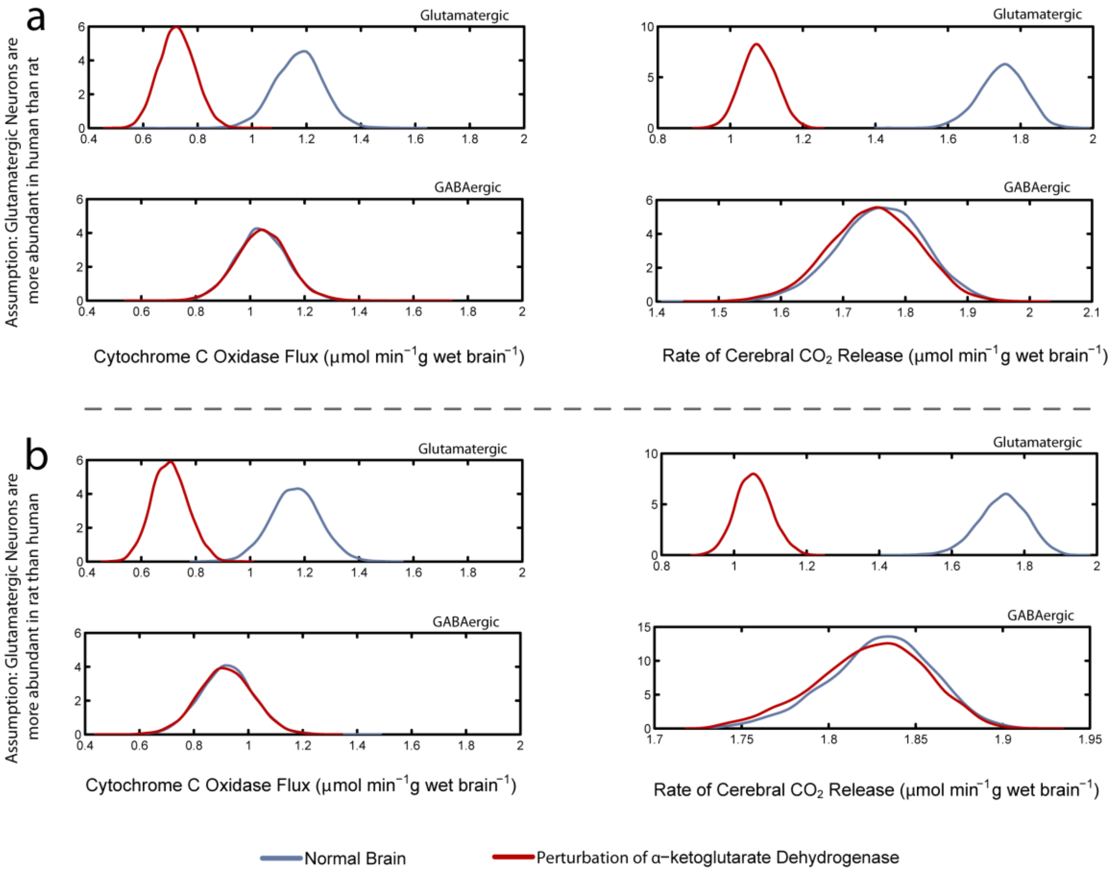

**Supplementary Figure 11. Results in this work are not affected by adjusting the rat glutamatergic/GABAergic neuron ratio.** The glutamatergic/GABAergic neuron ratio was varied, ranging from the assumption that glutamatergic neurons are more abundant in human than rats (a), to the assumption that they are more abundant in rat (b). As is apparent when comparing panels (a) and (b), this analysis demonstrates that there is almost no difference in the results, showing the robustness of this model result against variations in this parameter.

This analysis demonstrates that while it is expected that differences in these parameters are biologically meaningful *in vivo*, they are not governing constraints that affect the analyses in this work. However, future use of these parameters should, in like manner, be validated for robustness, since it is expected that these parameters will affect questions that compare astrocyte to neuron metabolism or that compare the levels of GABAergic and glutamatergic neurotransmission.

# References

1. Thiele, I., Price, N. D., Vo, T. D. & Palsson, B. O. Candidate metabolic network states in human mitochondria. Impact of diabetes, ischemia, and diet. *J. Biol. Chem.* **280**, 11683-11695 (2005).

2. Kaufman, D. E. & Smith, R. L. Direction Choice for Accelerated Convergence in Hit-and-Run Sampling. *OPERATIONS RESEARCH* **46**, 84-95 (1998).

3. Fukui, H., Diaz, F., Garcia, S. & Moraes, C. T. Cytochrome c oxidase deficiency in neurons decreases both oxidative stress and amyloid formation in a mouse model of Alzheimer's disease. *Proc. Natl. Acad. Sci. U. S. A.* **104**, 14163-14168 (2007).

4. Bubber, P., Haroutunian, V., Fisch, G., Blass, J. P. & Gibson, G. E. Mitochondrial abnormalities in Alzheimer brain: mechanistic implications. *Ann. Neurol.* **57**, 695-703 (2005).

5. Lying-Tunell, U., Lindblad, B. S., Malmlund, H. O. & Persson, B. Cerebral blood flow and metabolic rate of oxygen, glucose, lactate, pyruvate, ketone bodies and amino acids. *Acta Neurol. Scand.* **62**, 265-275 (1980).

6. Lying-Tunell, U., Lindblad, B. S., Malmlund, H. O. & Persson, B. Cerebral blood flow and metabolic rate of oxygen, glucose, lactate, pyruvate, ketone bodies and amino acids. *Acta Neurol. Scand.* **63**, 337-350 (1981).

7. Cakir, T., Alsan, S., Saybasili, H., Akin, A. & Ulgen, K. O. Reconstruction and flux analysis of coupling between metabolic pathways of astrocytes and neurons: application to cerebral hypoxia. *Theor. Biol. Med. Model.* **4**, 48 (2007).

8. Price, N. D., Thiele, I. & Palsson, B. O. Candidate states of Helicobacter pylori's genome-scale metabolic network upon application of "loop law" thermodynamic constraints. *Biophys. J.* **90**, 3919-3928 (2006).

9. Stuhmer, T., Anderson, S. A., Ekker, M. & Rubenstein, J. L. Ectopic expression of the Dlx genes induces glutamic acid decarboxylase and Dlx expression. *Development* **129**, 245-252 (2002).

10. MacDonald, R. B., Debiais-Thibaud, M., Talbot, J. C. & Ekker, M. The relationship between dlx and gad1 expression indicates highly conserved genetic pathways in the zebrafish forebrain. *Dev. Dyn.* **239**, 2298-2306 (2010).

11. Liang, W. S. *et al*. Altered neuronal gene expression in brain regions differentially affected by Alzheimer's disease: a reference data set. *Physiol. Genomics* **33**, 240-256 (2008).

12. Chatziioannou, A., Palaiologos, G. & Kolisis, F. N. Metabolic flux analysis as a tool for the elucidation of the metabolism of neurotransmitter glutamate. *Metab. Eng.* **5**, 201-210 (2003).

13. Occhipinti, R., Puchowicz, M. A., LaManna, J. C., Somersalo, E. & Calvetti, D. Statistical analysis of metabolic pathways of brain metabolism at steady state. *Ann. Biomed. Eng.* **35**, 886-902 (2007).

14. Orth, J. D. & Palsson, B. O. Systematizing the generation of missing metabolic knowledge. *Biotechnol. Bioeng.* (2010).

15. Feist, A. M. *et al*. A genome-scale metabolic reconstruction for Escherichia coli K-12 MG1655 that accounts for 1260 ORFs and thermodynamic information. *Mol. Syst. Biol.* **3**, 121 (2007).

16. Feist, A. M., Herrgard, M. J., Thiele, I., Reed, J. L. & Palsson, B. O. Reconstruction of biochemical networks in microorganisms. *Nat. Rev. Microbiol.* **7**, 129-143 (2009).

17. Thiele, I. & Palsson, B. O. A protocol for generating a high-quality genome-scale metabolic reconstruction. *Nat. Protocols* **5**, 93-121 (2010).

18. Satish Kumar, V., Dasika, M. S. & Maranas, C. D. Optimization based automated curation of metabolic reconstructions. *BMC Bioinformatics* **8**, 212 (2007).

19. Mo, M. L., Palsson, B. O. & Herrgard, M. J. Connecting extracellular metabolomic measurements to intracellular flux states in yeast. *BMC Syst. Biol.* **3**, 37 (2009).

20. Thiele, I., Jamshidi, N., Fleming, R. M. & Palsson, B. O. Genome-scale reconstruction of Escherichia coli's transcriptional and translational machinery: a knowledge base, its mathematical formulation, and its functional characterization. *PLoS Comput. Biol.* **5**, e1000312 (2009).

21. Purdon, A. D. & Rapoport, S. I. Energy requirements for two aspects of phospholipid metabolism in mammalian brain. *Biochem. J.* **335 ( Pt 2)**, 313-318 (1998).

22. Siegel, G. J. in *Basic neurochemistry : molecular, cellular, and medical aspects* 992 (Elsevier, Amsterdam ; Boston, 2006).

23. Rolfe, D. F. & Brown, G. C. Cellular energy utilization and molecular origin of standard metabolic rate in mammals. *Physiol. Rev.* **77**, 731-758 (1997).

24. Shen, J. *et al*. Determination of the rate of the glutamate/glutamine cycle in the human brain by in vivo 13C NMR. *Proc. Natl. Acad. Sci. U. S. A.* **96**, 8235-8240 (1999).

25. Gruetter, R., Seaquist, E. R. & Ugurbil, K. A mathematical model of compartmentalized neurotransmitter metabolism in the human brain. *Am. J. Physiol. Endocrinol. Metab.* **281**, E100-12 (2001).

26. Behar, K. L. & Rothman, D. L. In vivo nuclear magnetic resonance studies of glutamate-gamma-aminobutyric acid-glutamine cycling in rodent and human cortex: the central role of glutamine. *J. Nutr.* **131**, 2498S-504S; discussion 2523S-4S (2001).

27. Hassel, B., Johannessen, C. U., Sonnewald, U. & Fonnum, F. Quantification of the GABA shunt and the importance of the GABA shunt versus the 2-oxoglutarate dehydrogenase pathway in GABAergic neurons. *J. Neurochem.* **71**, 1511-1518 (1998).

28. Balazs, R., Machiyama, Y., Hammond, B. J., Julian, T. & Richter, D. The operation of the gamma-aminobutyrate bypath of the tricarboxylic acid cycle in brain tissue in vitro. *Biochem. J.* **116**, 445-461 (1970).

29. Xi, Y., Chen, Y. P., Qian, C. & Wang, F. Comparative study of computational methods to detect the correlated reaction sets in biochemical networks. *Brief Bioinform* (2010).

30. Shi, Q. *et al*. Responses of the mitochondrial alpha-ketoglutarate dehydrogenase complex to thiamine deficiency may contribute to regional selective vulnerability. *Neurochem. Int.* **50**, 921-931 (2007).

31. Burgard, A. P., Nikolaev, E. V., Schilling, C. H. & Maranas, C. D. Flux coupling analysis of genome-scale metabolic network reconstructions. *Genome Res.* **14**, 301-312 (2004).

32. Jamshidi, N. & Palsson, B. O. Investigating the metabolic capabilities of Mycobacterium tuberculosis H37Rv using the in silico strain iNJ661 and proposing alternative drug targets. *BMC Syst. Biol.* **1**, 26 (2007).

33. Schramm, G. *et al*. PathWave: discovering patterns of differentially regulated enzymes in metabolic pathways. *Bioinformatics* **26**, 1225-1231 (2010).

34. Benjamini, Y. & Yekutieli, D. The Control of the False Discovery Rate in Multiple Testing under Dependency. *The Annals of Statistics* **29**, 1165-1188 (2001).

35. Ibanez, V. *et al*. Regional glucose metabolic abnormalities are not the result of atrophy in Alzheimer's disease. *Neurology* **50**, 1585-1593 (1998).

36. Belmadani, A., Kumar, S., Schipma, M., Collins, M. A. & Neafsey, E. J. Inhibition of amyloid-beta-induced neurotoxicity and apoptosis by moderate ethanol preconditioning. *Neuroreport* **15**, 2093-2096 (2004).

37. Anttila, T. *et al*. Alcohol drinking in middle age and subsequent risk of mild cognitive impairment and dementia in old age: a prospective population based study. *BMJ* **329**, 539 (2004).

38. Ramesh, B. N., Rao, T. S., Prakasam, A., Sambamurti, K. & Rao, K. S. Neuronutrition and Alzheimer's disease. *J. Alzheimers Dis.* **19**, 1123-1139 (2010).

39. Panza, F., Capurso, C. & Solfrizzi, V. Alcohol use, thiamine deficiency, and cognitive impairment. *JAMA* **299**, 2853-4; author reply 2854-5 (2008).

40. Fillmore, K. M., Stockwell, T., Chikritzhs, T., Bostrom, A. & Kerr, W. Moderate alcohol use and reduced mortality risk: systematic error in prospective studies and new hypotheses. *Ann. Epidemiol.* **17**, S16-23 (2007).

41. Dudek, H. *et al*. The decrease in antioxidant potential in human brain tumours. *Rocz. Akad. Med. Bialymst.* **47**, 113-122 (2002).

42. Liang, W. S. *et al*. Alzheimer's disease is associated with reduced expression of energy metabolism genes in posterior cingulate neurons. *Proc. Natl. Acad. Sci. U. S. A.* **105**, 4441-4446 (2008).

43. Atamna, H. & Frey, W. H.,2nd. A role for heme in Alzheimer's disease: heme binds amyloid beta and has altered metabolism. *Proc. Natl. Acad. Sci. U. S. A.* **101**, 11153-11158 (2004).

44. Ghajar, J. B., Gibson, G. E. & Duffy, T. E. Regional acetylcholine metabolism in brain during acute hypoglycemia and recovery. *J. Neurochem.* **44**, 94-98 (1985).

45. Gibson, G. E., Jope, R. & Blass, J. P. Decreased synthesis of acetylcholine accompanying impaired oxidation of pyruvic acid in rat brain minces. *Biochem. J.* **148**, 17-23 (1975).

46. Chleide, E. & Ishikawa, K. Hypoxia-induced decrease of brain acetylcholine release detected by microdialysis. *Neuroreport* **1**, 197-199 (1990).

47. Cooper, J. R. Unsolved problems in the cholinergic nervous system. *J. Neurochem.* **63**, 395-399 (1994).

48. Ragozzino, M. E., Pal, S. N., Unick, K., Stefani, M. R. & Gold, P. E. Modulation of hippocampal acetylcholine release and spontaneous alternation scores by intrahippocampal glucose injections. *J. Neurosci.* **18**, 1595-1601 (1998).

49. Ragozzino, M. E., Unick, K. E. & Gold, P. E. Hippocampal acetylcholine release during memory testing in rats: augmentation by glucose. *Proc. Natl. Acad. Sci. U. S. A.* **93**, 4693-4698 (1996).

50. Stefani, M. R. & Gold, P. E. Intrahippocampal infusions of k-atp channel modulators influence spontaneous alternation performance: relationships to acetylcholine release in the hippocampus. *J. Neurosci.* **21**, 609-614 (2001).

51. Watson, G. S. & Craft, S. Modulation of memory by insulin and glucose: neuropsychological observations in Alzheimer's disease. *Eur. J. Pharmacol.* **490**, 97-113 (2004).

52. Lajtha, A., Gibson, G. E. & Dienel, G. A. in *Handbook of neurochemistry and molecular neurobiology. Brain energetics, integration of molecular and cellular processes* 924 (Springer, New York, 2007).

53. Ponten, F. *et al*. A global view of protein expression in human cells, tissues, and organs. *Mol. Syst. Biol.* **5**, 337 (2009).

54. Hershfield, J. R. *et al*. Aspartoacylase is a regulated nuclear-cytoplasmic enzyme. *FASEB J.* **20**, 2139-2141 (2006).

55. Szutowicz, A. & Lysiak, W. Regional and subcellular distribution of ATP-citrate lyase and other enzymes of acetyl-CoA metabolism in rat brain. *J. Neurochem.* **35**, 775-785 (1980).

56. Szutowicz, A., Stepien, M., Bielarczyk, H., Kabata, J. & Lysiak, W. ATP citrate lyase in cholinergic nerve endings. *Neurochem. Res.* **7**, 799-810 (1982).

57. Tucek, S., Dolezal, V. & Sullivan, A. C. Inhibition of the synthesis of acetylcholine in rat brain slices by (-)-hydroxycitrate and citrate. *J. Neurochem.* **36**, 1331-1337 (1981).

58. Kursula, P., Sikkila, H., Fukao, T., Kondo, N. & Wierenga, R. K. High resolution crystal structures of human cytosolic thiolase (CT): a comparison of the active sites of human CT, bacterial thiolase, and bacterial KAS I. *J. Mol. Biol.* **347**, 189-201 (2005).

59. Ohgami, M., Takahashi, N., Yamasaki, M. & Fukui, T. Expression of acetoacetyl-CoA synthetase, a novel cytosolic ketone body-utilizing enzyme, in human brain. *Biochem. Pharmacol.* **65**, 989-994 (2003).

60. Sterling, G. H., McCafferty, M. R. & O'Neill, J. J. beta-Hydroxybutyrate as a precursor to the acetyl moiety of acetylcholine. *J. Neurochem.* **37**, 1250-1259 (1981).

61. Ito, T. & Quastel, J. H. Acetoacetate metabolism in infant and adult rat brain in vitro. *Biochem. J.* **116**, 641-655 (1970).

62. Dolezal, V. & Tucek, S. Utilization of citrate, acetylcarnitine, acetate, pyruvate and glucose for the synthesis of acetylcholine in rat brain slices. *J. Neurochem.* **36**, 1323-1330 (1981).

63. White, H. L. & Scates, P. W. Acetyl-L-carnitine as a precursor of acetylcholine. *Neurochem. Res.* **15**, 597-601 (1990).

64. Guzman, M. & Blazquez, C. Is there an astrocyte-neuron ketone body shuttle? *Trends Endocrinol. Metab.* **12**, 169-173 (2001).

65. Gritti, I. *et al*. Stereological estimates of the basal forebrain cell population in the rat, including neurons containing choline acetyltransferase, glutamic acid decarboxylase or phosphate-activated glutaminase and colocalizing vesicular glutamate transporters. *Neuroscience* **143**, 1051-1064 (2006).

66. Itoh, Y., Abe, T., Takaoka, R. & Tanahashi, N. Fluorometric determination of glucose utilization in neurons in vitro and in vivo. *J. Cereb. Blood Flow Metab.* **24**, 993-1003 (2004).

67. Nedergaard, M., Ransom, B. & Goldman, S. A. New roles for astrocytes: redefining the functional architecture of the brain. *Trends Neurosci.* **26**, 523-530 (2003).